

Multidimensional Clutter Filter Optimization for Ultrasonic Perfusion Imaging

MinWoo Kim¹, Yang Zhu, Jamila Hedhli, Lawrence W. Dobrucki, and Michael F. Insana¹, *Fellow, IEEE*

Abstract—Combinations of novel pulse-echo acquisitions and clutter filtering techniques can improve the sensitivity and the specificity of power Doppler (PD) images, thus reducing the need for exogenous contrast enhancement. We acquire echoes following bursts of Doppler pulse transmissions sparsely applied in regular patterns over long durations. The goal is to increase the sensitivity of the acquisition to slow disorganized patterns of motion from the peripheral blood perfusion. To counter a concomitant increase in clutter signal power, we arrange the temporal echo acquisitions into two data-array axes, combine them with a spatial axis for the tissue region of interest, and apply 3-D singular-value decomposition (SVD) clutter filtering. Successful separation of blood echoes from other echo signal sources requires that we partition the 3-D SVD core tensor. Unfortunately, the clutter and blood subspaces do not completely uncouple in all situations, so we developed a statistical classifier that identifies the core tensor subspace dominated by tissue clutter power. This paper describes an approach to subspace partitioning as required for optimizing PD imaging of peripheral perfusion. The technique is validated using echo simulation, flow-phantom data, and *in vivo* data from a murine melanoma model. We find that for narrow eigen-bandwidth clutter signals, we can routinely map phantom flows and tumor perfusion signals at speeds less than 3 mL/min. The proposed method is well suited to peripheral perfusion imaging applications.

Index Terms—Higher order singular-value decomposition (HOSVD), peripheral perfusion imaging, source separation, subspace partitioning.

I. INTRODUCTION

PULSE-ECHO power Doppler (PD) imaging is highly sensitive to slow disorganized movements of red blood cells (RBCs), and therefore it is a natural choice for microvascular and perfusion imaging [1]. PD signals are insensitive to blood speed and direction but highly vulnerable to tissue clutter and acquisition noise sources. The most effective PD methods for perfusion imaging without contrast enhancement are those that maximize the sensitivity of echo signals to RBC movements in ways that can be uncoupled from clutter and noise signal sources. This report explores a new approach to perfusion imaging with a focus on clutter filter design.

Manuscript received April 15, 2018; accepted August 28, 2018. Date of publication September 3, 2018; date of current version November 7, 2018. (Corresponding author: Michael F. Insana.)

M. Kim is with the Department of Electrical and Computer Engineering, University of Illinois at Urbana-Champaign, Urbana, IL 61801 USA (e-mail: mkim180@illinois.edu).

Y. Zhu, J. Hedhli, L. W. Dobrucki, and M. F. Insana are with the Department of Bioengineering, Beckman Institute for Advanced Science and Technology, University of Illinois at Urbana-Champaign, Urbana, IL 61801 USA (e-mail: yangzhu2@illinois.edu; hedhli2@illinois.edu;dobrucki@illinois.edu; mfi@illinois.edu).

Digital Object Identifier 10.1109/TUFFC.2018.2868441

Detailed overviews of clutter filtering research are found in [2] and [3]. Originally, Fourier-basis clutter filters were applied, e.g., finite-impulse response, IIR. The Doppler equation provided a direct interpretation between the temporal Fourier coefficients and the blood velocity. However, it is now well accepted that Fourier-basis filters do not provide the best separation between the tissue and the slow-moving blood echoes [3]–[5]. Eigenbases are a generalization of Fourier bases that can adapt to specific data sets and thus have the potential to provide more separability between the blood and tissue subspaces. Eigenfilters result from a decomposition of the echo data temporal correlation matrix. In contrast, singular-value decomposition (SVD)-basis filters are able to fully exploit the spatiotemporal nature of each echo acquisition [6]–[9]. The 2-D SVD generates both the temporal and spatial bases so that the characteristically strong echoes of spatially coherent tissue movements can be more readily separated from the weaker echoes of spatially incoherent blood perfusion echoes.

Recently, high frame-rate acquisition techniques have been coupled to 2-D SVD clutter filters to provide exciting new opportunities for microvascular imaging in brain, kidney, and thyroid tissues [9], [10]. Attempts to reduce the computational cost when filtering huge data volumes have also been presented [11]–[13]. We are developing peripheral muscle perfusion imaging to assess microvascular damage from ischemia and chronic metabolic disorders [14]. For our task, the blood flow is steady and nonstationary clutter echoes arise mostly from small-amplitude muscle vibration and transducer motion.

We found previously that probing tissues with bursts of multicycle Doppler pulses over long durations can significantly increase the sensitivity of echo signals to peripheral perfusion RBC movement [15]. RBC sensitivity increases if we reorder the time axis into two array dimensions, labeled slow-time and frame-time axes, to produce a 3-D echo-data array. The 3-D data arrays are decomposed using higher order SVD (HOSVD) techniques [16]–[18] to produce three orthogonal basis sets corresponding to slow-time, spatial, and frame-time vector spaces. We also found that enhanced perfusion signals could be uncoupled from clutter by decomposing the data array and locating the blood subspace within the 3-D core tensor elements [15]. However, subsequent phantom studies reported in the following suggest the eigen-bandwidth for clutter plays a key role in clutter-blood subspace separability.

The purpose of this report is to propose a statistical classifier that, when applied to each core tensor element, can identify the eigen-bandwidth for clutter filter design. The classifier

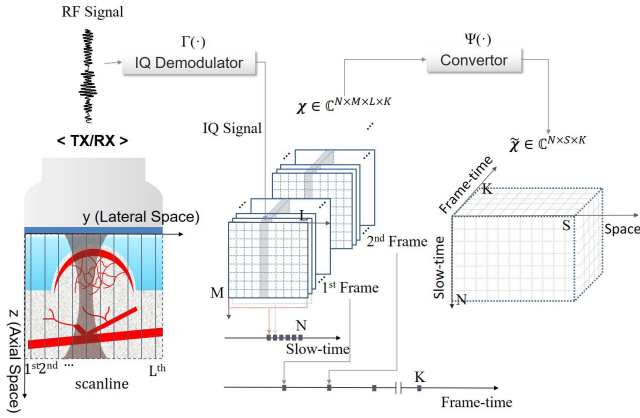


Fig. 1. Color-flow acquisition is illustrated resulting in multidimensional data array \mathcal{X} . A linear array transmits sound pulses into tissue and receives echoes along a line of site. Signals from the receive aperture are beamformed, fast-time sampled, decomposed into baseband quadrature signals and stored as an M -point complex IQ vector. N transmissions in slow time at a ~ 1 -kHz pulse repetition frequency are made for each of L lateral lines to compose one 3-D Doppler frame. Recording K frames at a ~ 10 -Hz frame repetition frequency yields the 4-D data array $\mathcal{X} \in \mathbb{C}^{N \times M \times L \times K}$. The 4-D array is reordered to form 3-D array $\tilde{\mathcal{X}} \in \mathbb{C}^{N \times S \times K}$, where $S = ML$.

decides if a core element is predominantly from a clutter source based on a vector of five signal energy and similarity features estimated from the decomposition eigenvalues and eigenvectors. Encouraged by a similar approach described by Baranger *et al.* [10] for 2-D SVD filters, we arrive at different but consistent findings. Signal subspaces and clutter filter designs are explored through echo simulations, where all data properties are known exactly, phantom experiments, where data properties are known statistically, and *in vivo* experiments, where the data properties are most realistic.

II. METHODS

A. Notation

To distinguish various types of data arrays, we adopt the following notation.

- 1) Scalars are lower case or capital letters $a, b, N, M \dots$
- 2) Column vectors are bold lower case letters $\mathbf{a}, \mathbf{b} \dots$
- 3) Matrices are bold capital letters $\mathbf{A}, \mathbf{B} \dots$
- 4) Multidimensional arrays (tensors) are bold calligraphic capital letters $\mathcal{A}, \mathcal{B} \dots$
- 5) *Array elements*: The i th element of vector \mathbf{a} is denoted by $a_i = \mathbf{a}[i]$, the (i_1, i_2) th element of matrix \mathbf{A} is $a_{i_1, i_2} = \mathbf{A}[i_1, i_2]$, and the (i_1, i_2, i_3) th element of 3-D array (tensor [17]) \mathcal{A} is $a_{i_1, i_2, i_3} = \mathcal{A}[i_1, i_2, i_3] = \mathcal{A}_{i_1, i_2, i_3}$.

Sets for integers, real numbers, and complex numbers are represented as \mathbb{Z} , \mathbb{R} , and \mathbb{C} , respectively. For example, $a \in \mathbb{Z}_{[0, N]}$ indicates a is an integer scalar and $0 \leq a \leq N$.

B. Echo Signal Model

First, we define the spatiotemporal structure of the data array resulting from the narrowband PD acquisition illustrated in Fig. 1. Each beamformed quadrature [in-phase and quadrature (IQ)] echo waveform $x(t)$ is sampled on the fast-time interval T as $x(t_m)$ where $t_m = mT$ and $m \in \mathbb{Z}_{[1, M]}$. M is the number of temporal samples recorded following each

pulse transmission. Scaling the time axis, we form the axial waveform $x(z_m) = x(z_0 + ct_m/2)$ where c is the sound speed and z_0 is the distance between the transducer surface and the onset of the range gate. Repeatedly transmitting N pulses at each line of site on the slow-time interval $T' > MT$ results in 2-D spatiotemporal echo signal $x(t_n, z_m)$, where $t_n = nT'$ and $n \in \mathbb{Z}_{[1, N]}$. Scanning laterally, we record L echo lines separated by interval D within each frame. The 3-D Doppler frame $x(t_n, z_m, y_l)$ has a slow-time dimension and two spatial dimensions including y_l as the lateral position of the l th echo line; $l \in \mathbb{Z}_{[1, L]}$. Finally, K Doppler frames are recorded at frame-time interval $T'' > T'$ to form the 4-D echo-data array

$$\mathcal{X} = x(t_n, z_m, y_l, t_k) \in \mathbb{C}^{N \times M \times L \times K} \quad (1)$$

where $t_k = kT''$ and $k \in \mathbb{Z}_{[1, K]}$.

Second, we describe a linear model for simulating (1). Echoes from perfused tissues are assumed to arise from discrete RBC and surrounding tissue reflectors, the latter is referred to as tissue clutter. Discrete acquisition time $t = t_{n, m, l, k}$ is the clock time passing during a complete 4-D acquisition. Scattering functions $c_i(z, y, t)$ and $b_j(z, y, t)$ define the i th discrete tissue reflector and the j th RBC, respectively, at spatiotemporal location (z, y, t) . Furthermore, let $h(z, y)$ be the spatially invariant pulse-echo impulse response of the ultrasonic instrument. Consequently, the echo-data array \mathcal{X} can be modeled as a 2-D spatial convolution

$$\begin{aligned} \mathcal{X}_{n, m, l, k} = & \Gamma \left(\iint_{\Omega} dz dy h(z - (z_0 + cmT/2), y - y_l) \right. \\ & \left. \times \left[\sum_{i=1}^{J_c} c_i(z, y, t_{n, m, l, k}) + \sum_{j=1}^{J_b} b_j(z, y, t_{n, m, l, k}) \right] \right) \\ & + e_{n, m, l, k} \end{aligned} \quad (2)$$

where $\Gamma(\cdot)$ is the operator that converts RF signals to IQ components [19], Ω is a 2-D region indicating the spatial extent of the acquisition (the M and L dimensions in Fig. 1), and J_c and J_b are the number of discrete tissue and blood scatterers, respectively, in Ω . Also, e is additive white-Gaussian acquisition noise. Equation (2) is more simply expressed as the sum of three 4-D arrays describing clutter \mathcal{C} , blood \mathcal{B} , and noise \mathcal{N} sources via

$$\mathcal{X} = \mathcal{C} + \mathcal{B} + \mathcal{N}. \quad (3)$$

Ratios of signal power between the contributing sources are

$$\begin{cases} r_{CB} = 10 \log_{10}(\|\mathcal{C}\|^2 / \|\mathcal{B}\|^2) \\ r_{BN} = 10 \log_{10}(\|\mathcal{B}\|^2 / \|\mathcal{N}\|^2) \end{cases} \quad (4)$$

where $\|\cdot\|$ indicates the ℓ_2 -norm and r_{CB} and r_{BN} are clutter-to-blood and blood-to-noise ratios, respectively, each expressed in decibels.

C. Tissue and Blood Motion

The i th tissue scatterer randomly positioned in $\Omega_c \in \Omega$ (see Fig. 2) is represented by the Dirac delta

$$c_i(z, y, t) = \alpha_c^{(i)} \delta(z - (z_{c0} + z_c(t))^{(i)}, y - (y_{c0} + y_c(t))^{(i)}) \quad (5)$$

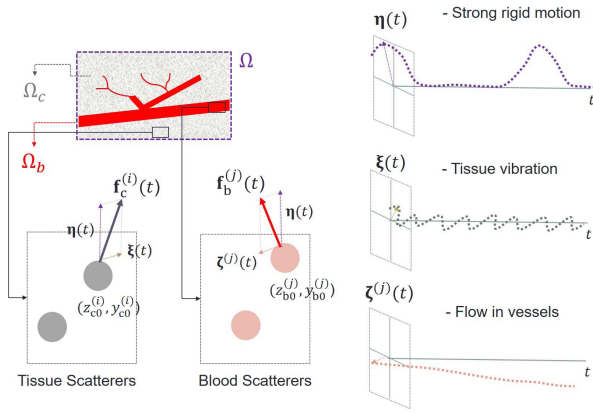


Fig. 2. Simulation of tissue perfusion is illustrated. Scattering field Ω consists of nonoverlapping regions of tissue scatterers in Ω_c and moving RBCs in Ω_b . A time series (top right) for the entire field Ω in which all scatterers (bottom left) undergo large-scale low-frequency periodic rigid motion mimicking respiration. In addition, scatterers in regions Ω_c undergo rigid-body vibration at higher frequency and smaller amplitude, while vascular RBCs in regions Ω_b undergo blunt-flow translation with known velocity.

where $\alpha_c^{(i)} \sim N(m_{\alpha_c}, \sigma_{\alpha_c}^2)$ is a normally distributed echo amplitude assigned to the i th tissue scatterer, and (z_{c0}, y_{c0}) is its position in Ω_c at $t = 0$. Tissue displacement vector $\mathbf{f}_c^{(i)}(t)$, which applies at $t > 0$, describes the temporal movements of all tissue scatterers in Ω relative to the initial positions. It includes the sum of 2-D breathing $\boldsymbol{\eta}(t)$ and muscle vibration $\boldsymbol{\xi}(t)$ vectors

$$\mathbf{f}_c^{(i)}(t) = (z_c(t), y_c(t))^{(i)} = \boldsymbol{\eta}(t) + \boldsymbol{\xi}(t) \quad \text{for } t > 0$$

and where

$$\begin{cases} \boldsymbol{\eta}(t) = \beta \left[\sum_{n'} e^{-\frac{(t-n'\Delta t)^2}{2\sigma_r^2}}, 0 \right] \\ \boldsymbol{\xi}(t) = \gamma \sin(w_0 t) [\cos(\theta), \sin(\theta)]. \end{cases} \quad (6)$$

Symbol n' is an integer, Δt indicates the interval between breaths, and β and σ_r specify the range and rate of breathing movement oriented along the z -axis. Parameters γ , w_0 , and θ determine the oscillation strength, frequency, and direction, of muscle vibration. The directions of the two sources of clutter movement are neither aligned to each other nor they are synchronous, although each function is applied simultaneously to all scatterers in Ω_c .

Similarly, the position of the j th RBC is

$$b_j(z, y, t) = \alpha_b^{(j)} \delta(z - (z_{b0} + z_b(t))^{(j)}, y - (y_{b0} + y_b(t))^{(j)}) \quad (7)$$

where the RBC echo amplitude is $\alpha_b^{(j)} \sim N(m_{\alpha_b}, \sigma_{\alpha_b}^2)$ and (z_{b0}, y_{b0}) is the initial position within $\Omega_b \in \Omega$.

Blood displacement vector $\mathbf{f}_b^{(j)}(t) = (z_b^{(j)}(t), y_b^{(j)}(t))$ describes the temporal movement of the j th RBC at times $t > 0$ relative to its initial position. RBC movement is also modeled as the sum of two 2-D vector sources

$$\mathbf{f}_b^{(j)}(t) = \boldsymbol{\eta}(t) + \boldsymbol{\zeta}^{(j)}(t) \quad \text{for } t > 0$$

where

$$\boldsymbol{\zeta}^{(j)}(t) = t[|v^{(j)}| \sin \varphi^{(j)}, |v^{(j)}| \cos \varphi^{(j)}]. \quad (8)$$

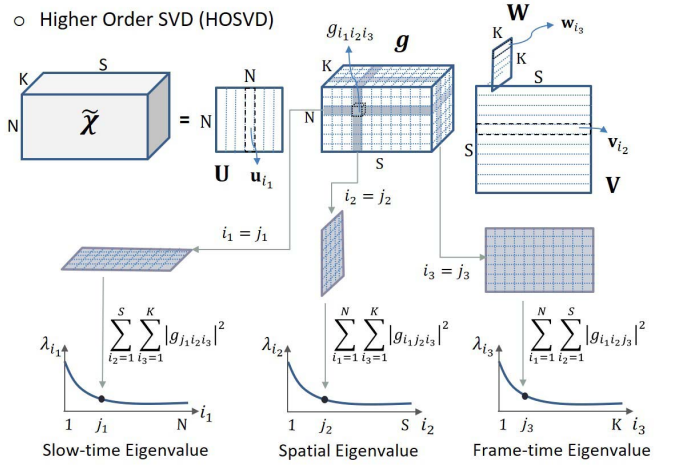


Fig. 3. Decomposition of 3-D data array $\tilde{\mathcal{X}}$ using HOSVD is illustrated. Element g_{i_1, i_2, i_3} is an element of the 3-D core tensor \mathcal{G} . That element is associated with slow-time eigenvector \mathbf{u}_{i_1} and eigenvalue λ_{i_1} , spatial eigenvector \mathbf{v}_{i_2} and eigenvalue λ_{i_2} , and frame-time eigenvector \mathbf{w}_{i_3} and eigenvalue λ_{i_3} .

The speed $|v^{(j)}|$ and the Doppler angle $\varphi^{(j)}$ are constant in time but vary spatially within Ω as illustrated, e.g., by the vascular patterns in Fig. 2. Since respiration is a rigid-body translation of vessels with the surrounding tissues, $\boldsymbol{\eta}(t)$ is the same as that given in (6).

Equations (6) and (8) update (5) and (7) at each time interval. The results of (5) and (7) are summed in (2) and convolved with impulse response $h(z, y)$ to simulate RF echo signals. In this study, $h(z, y)$ is a shift invariant, 2-D Gaussian pulse with sinusoidally modulated amplitude along the z -axis. The IQ components of the RF echo signals composing the 4-D complex-valued array $\mathcal{X}_{n,m,l,k}$ are found by demodulating the analytic RF echo signals [19], as shown in (2).

D. Decomposition of Data Array $\tilde{\mathcal{X}}$

The slow-time dimension of data array \mathcal{X} , with values sampled on the order of kilohertz, is most sensitive to echoes from fast vascular flows. Its frame-time dimension, sampled on the order of hertz, is most sensitive to slow spatially incoherent perfusion echoes. The two spatial dimensions provide essential information about the spatiotemporal heterogeneity of primarily tissue echoes. Both the spatial axes can be reordered into a single array axis dimension for the purpose of building a clutter filter. We do this by applying lexicographic transformation operator Ψ , resulting in

$$\tilde{\mathcal{X}} = \Psi(\mathcal{X}), \quad \text{such that } \tilde{x}_{n,s,k} = x_{n,m,l,k} \quad (9)$$

where $\tilde{\mathcal{X}} \in \mathbb{C}^{N \times S \times K}$, $s = m + (l-1)M$, and $S = ML$. We showed previously [15] how to decompose $\tilde{\mathcal{X}}$ using HOSVD. Reducing the data array from 4-D to 3-D speeds the HOSVD compute time.

HOSVD is a multilinear generalization of 2-D SVD analysis [16], [18]. As illustrated in Fig. 3, decomposing $\tilde{\mathcal{X}}$ generates core tensor¹ $\mathcal{G} \in \mathbb{C}^{N \times S \times K}$ with core elements g_{i_1, i_2, i_3} and three orthogonal matrices: $\mathbf{U} \in \mathbb{C}^{N \times N}$ whose

¹Modal planes in \mathcal{G} are orthogonal; i.e., $\sum_{i_1} \sum_{i_2} g_{i_1, i_2, a} g_{i_1, i_2, b} = \sum_{i_1} \sum_{i_3} g_{i_1, a, i_3} g_{i_1, b, i_3} = \sum_{i_2} \sum_{i_3} g_{a, i_2, i_3} g_{b, i_2, i_3} = 0$ unless $a = b$.

columns \mathbf{u} are slow-time-mode eigenvectors, $\mathbf{V} \in \mathbb{C}^{S \times S}$ whose columns \mathbf{v} are spatial-mode eigenvectors, and $\mathbf{W} \in \mathbb{C}^{K \times K}$ whose columns \mathbf{w} are frame-time-mode eigenvectors. The expression is [15]

$$\begin{aligned} \tilde{\mathcal{X}} &= \mathcal{G} \times_1 \mathbf{U} \times_2 \mathbf{V} \times_3 \mathbf{W} \\ &= \sum_{i_1=1}^N \sum_{i_2=1}^S \sum_{i_3=1}^K g_{i_1, i_2, i_3} \mathbf{u}_{i_1} \times \mathbf{v}_{i_2} \times \mathbf{w}_{i_3} \end{aligned} \quad (10)$$

where \times_n denotes n -mode outer product as defined in [15], [16], and [18]. The eigenvalues for each of the three modes are given as

$$\left\{ \begin{array}{l} \text{Slow-time mode: } \lambda_{j_1}^{(1)} = \sum_{i_2=1}^S \sum_{i_3=1}^K |g_{j_1, i_2, i_3}|^2 \\ \text{Spatial mode: } \lambda_{j_2}^{(2)} = \sum_{i_1=1}^N \sum_{i_3=1}^K |g_{i_1, j_2, i_3}|^2 \\ \text{Frame-time mode: } \lambda_{j_3}^{(3)} = \sum_{i_1=1}^N \sum_{i_2=1}^S |g_{i_1, i_2, j_3}|^2. \end{array} \right. \quad (11)$$

Eigenvalues for each mode are arranged in decreasing order.

Our main interest is to preserve echo signals originating from blood perfusion while suppressing other echo signal contributions. We can filter the echo data by identifying the 3-D subspace in \mathcal{G} dominated by perfusion echoes and suppressing values outside the perfusion subspace. Since signal power from clutter, blood, and acquisition-noise sources can occupy the same subspace, the filtering process is not straightforward.

E. Clutter Filtering

The strategy is to classify each core element (i_1, i_2, i_3) as clutter or nonclutter based on five features described in the following. Elements identified as ‘‘clutter dominant’’ are discarded.

1) Feature Selection:

a) *Normalized Eigenvalues:* Three of the five features are from the normalized eigenvalue spectra. The slow-time eigenvalue spectrum is normalized using

$$\bar{\lambda}_{i_1}^{(1)} = \frac{\log_{10} \lambda_{i_1}^{(1)} - \log_{10} \lambda_{\min}^{(1)}}{\log_{10} \lambda_{\max}^{(1)} - \log_{10} \lambda_{\min}^{(1)}} \in \mathbb{R}_{[0,1]} \quad (12)$$

where $\lambda_{\max}^{(1)} = \lambda_1^{(1)}$ and $\lambda_{\min}^{(1)} = \lambda_N^{(1)}$. Similarly, the normalized spatial and frame-time eigenvalue spectra are $\bar{\lambda}_{i_2}^{(2)}$ and $\bar{\lambda}_{i_3}^{(3)}$, respectively. In each normalized spectrum, the first value is largest and equal to 1. When the clutter is significant, subsequent spectral values at $i_1, i_2, i_3 > 1$ associated with clutter remain close to 1 (Fig. 4, top right). Large eigenvalues arise from the most echogenic components of $\tilde{\mathcal{X}}$ that are typically associated with stationary or rigid-body tissues dynamics.

b) *Tissue Structure Similarity:* The magnitude of each spatial eigenvector, $\mathbf{s}_{i_2} = |\mathbf{v}_{i_2}| \in \mathbb{R}^{S \times 1}$, which are columns of \mathbf{V} , can be reformatted into a 2-D image $\mathbf{S}_{i_2} \in \mathbb{R}^{M \times L}$. Eigen image \mathbf{S}_1 is associated with the largest (first) eigenvalue. It resembles the B-mode image for the region of interest. Other eigen images from \mathbf{V}

which are influenced by tissue clutter will have similar structural patterns. In contrast, eigen images most influenced by blood signals or noise will appear dissimilar to \mathbf{S}_1 . The fourth feature, d , compares the first eigen image with each of the others using Pearson’s correlation coefficient via operator $\Upsilon(\cdot)$ to quantify similarity

$$\begin{aligned} d_{i_2} &= \Upsilon(\mathbf{s}_1, \mathbf{s}_{i_2}) \\ &= \frac{\sum_{n=1}^S (\mathbf{s}_1[n] - \bar{s}_1)(\mathbf{s}_{i_2}[n] - \bar{s}_{i_2})}{\sqrt{\sum_{n=1}^S (\mathbf{s}_1[n] - \bar{s}_1)^2} \sqrt{\sum_{n=1}^S (\mathbf{s}_{i_2}[n] - \bar{s}_{i_2})^2}} \end{aligned} \quad (13)$$

where $d_{i_2} \in \mathbb{R}_{[-1,1]}$, and \bar{s}_1, \bar{s}_{i_2} are the means of all samples in vectors $\mathbf{s}_1, \mathbf{s}_{i_2}$. Large positive d values indicate core elements with significant clutter contributions to $\tilde{\mathcal{X}}$ (see Fig. 4, right).

c) *Rigid-Body Motion Corruption:* Adding a frame axis to extend the echo-data array enhances the sensitivity to both the blood perfusion and the moving tissue clutter. The magnitude of motion over the frame-time axis is identified by comparing echo power images obtained from the k th Doppler frame using

$$\mathbf{P}_k[m, \ell] = 10 \log_{10} \left(\frac{1}{N} \sum_{n=1}^N |\mathcal{X}[n, m, \ell, k]|^2 \right). \quad (14)$$

The similarity between the echo power in two frames is

$$\mathbf{Q}[j, k] = \Upsilon(\mathbf{P}_j, \mathbf{P}_k) \quad (15)$$

where matrix $\mathbf{Q} \in \mathbb{R}^{K \times K}$. The sudden, large-amplitude, coherent motion characteristic of clutter creates distinct patterns in \mathbf{Q} (see Fig. 4, right) where echo power is far less correlated. Negative correlations are possible, but, in practice, correlations from rigid-body motion remain positive. The mean correlation between the k th and j th frames is

$$\mathbf{q}[k] = \frac{1}{K} \sum_{j=1}^K \mathbf{Q}[j, k] \in \mathbb{R}_{[0,1]}. \quad (16)$$

Large coherent displacements, like those from breathing, result in small correlation values. Vector \mathbf{q} can thus be used as a basis to test if a frame is corrupted by clutter motion. The inner product

$$r_{i_3} = \sum_{k=1}^K \mathbf{q}[k] |\mathbf{w}_{i_3}[k]|^2 \in \mathbb{R}_{[0,1]} \quad (17)$$

provides r , a scalar feature quantifying motion corruption in a data frame. Note that $|\mathbf{w}_{i_3}[k]|^2$ results from a Hadamard (elementwise) product of \mathbf{w}_{i_3} with itself. Small values of r indicate a frame is corrupted by coherent motion.

Each core tensor element is classified based on the feature vector \mathbf{z} computed for that element, from (12), (13) and (17)

$$\mathbf{z}_{i_1, i_2, i_3} = [\bar{\lambda}_{i_1}^{(1)}, \bar{\lambda}_{i_2}^{(2)}, \bar{\lambda}_{i_3}^{(3)}, d_{i_2}, r_{i_3}]^T. \quad (18)$$

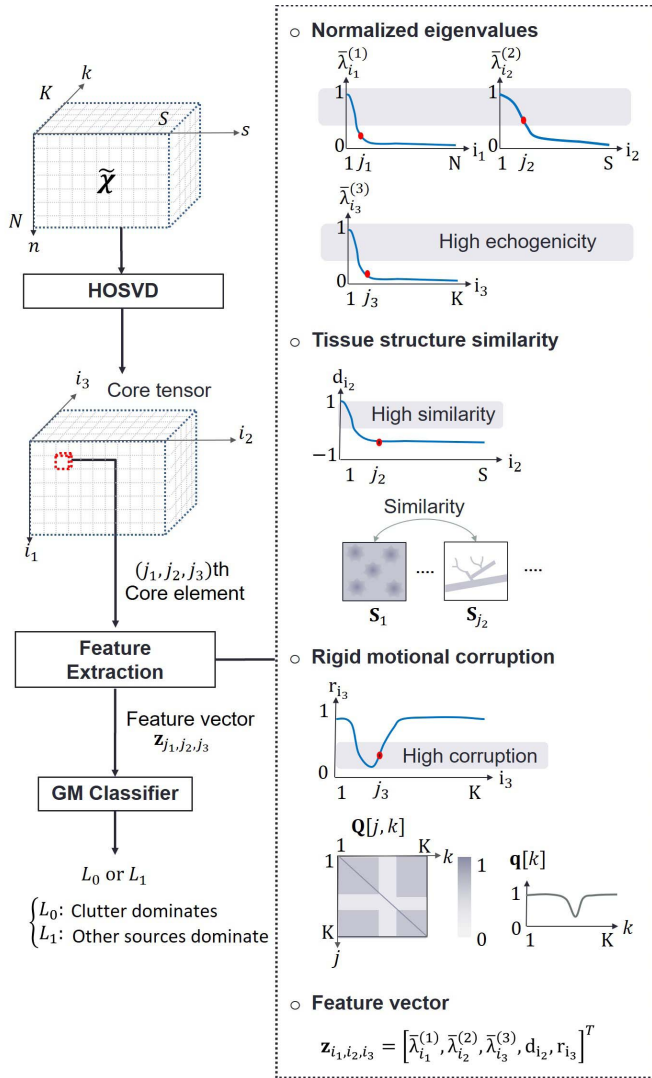


Fig. 4. Classification of each eigenelement for clutter filtering. To determine the state of (j_1, j_2, j_3) th core element, features are extracted from eigenvectors and eigenvalues. Normalized eigenvalues are associated with source echogenicity. The eigen image using spatial eigenvector provides structural information as shown in Fig. 6. Provided that first eigen image S_1 most likely involves tissue structure, the correlation between the first image and j_2 th image informs the contribution of the j_2 th eigenspace for tissue clutter. The last feature is associated with strong rigid motion. Data acquired for the moment tend to be corrupted by strong clutter. The time points can be recognized by similarity matrix Q obtained by computing the correlation between frame images. The feature measures the contribution of the j_3 th eigenspace for the time points (corruption). The GM classifier makes a decision using the features.

2) *GM Classifier*: Each core element was classified as clutter dominated L_0 or nonclutter dominated L_1 using the following likelihood ratio test classifier:

$$D(\mathbf{z}) = \begin{cases} L_0, & \text{if } p(\mathbf{z}|L_0)/p(\mathbf{z}|L_1) > \tau \\ L_1, & \text{if } p(\mathbf{z}|L_0)/p(\mathbf{z}|L_1) \leq \tau. \end{cases} \quad (19)$$

Threshold τ depends on error risks [20], which can be determined once the clinical task is defined. $p(\mathbf{z}|L_0)$ and $p(\mathbf{z}|L_1)$ are probability density functions (pdfs) conditioned on states L_0 and L_1 , viz., $p(\mathbf{z}|L_i) \sim \text{Normal}(\bar{\mathbf{z}}_i, \Sigma_i)$, $i \in \{0, 1\}$. We will show that both pdfs are found by applying training data.

From simulated echo data with known states, likelihood functions are modeled as linear mixtures of three multivariate Gaussian functions [Gaussian mixture (GM) models]

$$p(\mathbf{z}|L_i) = \sum_{j=1}^3 A_{ij} \frac{1}{\sqrt{(2\pi)^3 |\Sigma_{ij}|}} e^{-\frac{1}{2}(\mathbf{z}-\bar{\mathbf{z}}_{ij})^\dagger \Sigma_{ij}^{-1} (\mathbf{z}-\bar{\mathbf{z}}_{ij})} \quad (20)$$

where \mathbf{z}^\dagger is the conjugate transpose of \mathbf{z} . Amplitudes A_{ij} , mean vectors $\bar{\mathbf{z}}_{ij}$, and covariance matrices Σ_{ij} are for the i th state and the j th (of three) mixture model functions. A three-component mixture model was found to provide an acceptable compromise between the model accuracy and the computation time as discussed in Section III-A.

3) *Training*: Simulated echo signals are computed from training media similar to the perfused tissue regions illustrated in Figs. 1 and 2. First, we set the blood and noise terms to zero in (2) to compute the clutter-only component, $\mathcal{C} \in \mathbb{C}^{N \times M \times L \times K}$, and reformat the result via (9) to find $\tilde{\mathcal{C}} \in \mathbb{C}^{N \times S \times K}$. Next, (2) is applied to the same model, now including all scattering components, to simulate perfusion data \mathcal{X} with clutter and noise. The 4-D array is reformatted to find $\tilde{\mathcal{X}} \in \mathbb{C}^{N \times S \times K}$ and decomposed with HOSVD to compute core tensor $\mathcal{G} \in \mathbb{C}^{N \times S \times K}$. Rectangular subspaces within \mathcal{G} of increasing size, beginning with element $i_1 = i_2 = i_3 = 1$ and growing to $i_1 = N, i_2 = S, i_3 = K$, are progressively selected to form all possible estimates of clutter subspace $\hat{\mathcal{G}}_C$. Core elements outside the selected regions are set to zero. Reconstructing the echo data matrix from (10), but using $\hat{\mathcal{G}}_C$ in place of \mathcal{G} , we estimate the clutter-only signal, $\hat{\mathcal{C}}$. Subspace $\hat{\mathcal{G}}_C$ giving clutter echo signal estimate $\hat{\mathcal{C}}$ that most closely matches the known clutter-only signal $\tilde{\mathcal{C}}$ becomes the final subspace estimate, \mathcal{G}_C . The objective function is

$$\mathcal{G}_C = \arg \min_{\hat{\mathcal{G}}_C} \|\tilde{\mathcal{C}} - \hat{\mathcal{C}}\|^2$$

$$\text{w.r.t.} \begin{cases} \hat{\mathcal{C}} = \sum_{(i_1, i_2, i_3) \in \hat{\mathcal{G}}_C} g_{i_1, i_2, i_3} \mathbf{u}_{i_1} \times \mathbf{v}_{i_2} \times \mathbf{w}_{i_3} \\ \hat{\mathcal{G}}_C = \{(i_1, i_2, i_3) | 0 < i_1 < c_{i_1}, \\ 0 < i_2 < c_{i_2}, 0 < i_3 < c_{i_3}\}. \end{cases} \quad (21)$$

The feature vectors for core elements within \mathcal{G}_C are labeled L_0 , others are labeled L_1 . Training results in a hard threshold being set for subspace parsing.

4) *Testing*: With the knowledge of the clutter subspace from (21), we can estimate the parameters in (20). Specifically, equivalent Matlab R2015b functions “gmdistribution.fit” or “fitgmdist” apply the expectation-maximization algorithm to find maximum-likelihood estimates of the three-component GM model parameters, A_{ij} , $\bar{\mathbf{z}}_{ij}$, and Σ_{ij} . Finally, combining (19) and (20), we are now prepared to simulate the test data (independent of the training data) to test this clutter filter. First, we discuss a method for filtering acquisition noise.

F. Noise Filtering

Several techniques for suppressing additive white-Gaussian noise in a data array have been thoroughly studied [21]–[23]. Following clutter filtering, the noise-filtering approach we

adopt is to find the blood-signal rank for the correlation matrix of each data-array mode, r_i , and to zero eigenvalues beyond r_i . In a tensor model, the blood-signal rank can be different for the slow-time, spatial, and frame-time correlation matrices. We adopt a minimum description length method for estimating the blood-signal rank of each matrix [21]. For example, the rank of the slow-time correlation matrix is estimated as

$$r_1 = \arg \min_r -2 \log \left\{ \frac{\prod_{i=r+1}^N [\lambda_i^{(1)}]^{1/(M-r)}}{\frac{1}{M-r} \sum_{i=r+1}^M \lambda_i^{(1)}} \right\}^{SK(M-r)} + r(2M-r) \log(SK). \quad (22)$$

Similarly, we estimate r_2 and r_3 . Data are noise filtered by discarding the noise-dominated subspace using the hard threshold $\mathcal{G}_N = \{i_1, i_2, i_3 | (i_1 > r_1) \vee (i_2 > r_2) \vee (i_3 > r_3)\}$ where \vee indicates logical “or.” What remains is the blood subspace \mathcal{G}_B .

G. Velocity Discrimination

We found that the slow-time eigenvector can be used to parse speed ranges for blood components of the postfiltered echo signal. The frequency spectrum of each slow-time eigenvector is found using the discrete Fourier transform expression

$$U[k] = \left| \frac{1}{N} \sum_{n=1}^N u_{i_1}[n] \exp(-i2\pi nk/N) \right| \quad (23)$$

where $u_{i_1}[n]$ is a n th element of eigenvector \mathbf{u}_{i_1} . The slow-time frequency $f = k/NT'$ is converted into the axial component of blood speed v using the Doppler equation $v = cf/2f_c$, where c and f_c are the wave speed and the pulse center frequency, respectively. The weight indicating contributions to the eigenvector from the speed range $[v_{\min}, v_{\max}]$ is found from

$$\omega_{i_1} = \sum_k U[k]w[k] \\ w[k] = \begin{cases} 1, & \text{if } v_{\min} < \left| \frac{cf}{2f_c} \right| < v_{\max} \\ 0, & \text{otherwise.} \end{cases} \quad (24)$$

The weight is used to apply a soft-threshold in the slow-time mode.

Velocity discrimination combined with clutter and noise suppression yields an estimate of the target blood-echo signal

$$\hat{\mathcal{B}} = \sum_{(i_1, i_2, i_3) \in \mathcal{G}_B} g_{i_1, i_2, i_3} (\omega_{i_1} \mathbf{u}_{i_1}) \times \mathbf{v}_{i_2} \times \mathbf{w}_{i_3}. \quad (25)$$

H. Filter Scale

Echo frames up to several square centimeters in the area are recorded for as long as 10 s to capture the blood perfusion patterns. However, the heterogeneous space-time properties of tissue suggest that one filter cannot be expected to apply to all data in an acquisition. Instead, we divide data arrays into statistically homogeneous blocks that may overlap, and we develop filters for each.

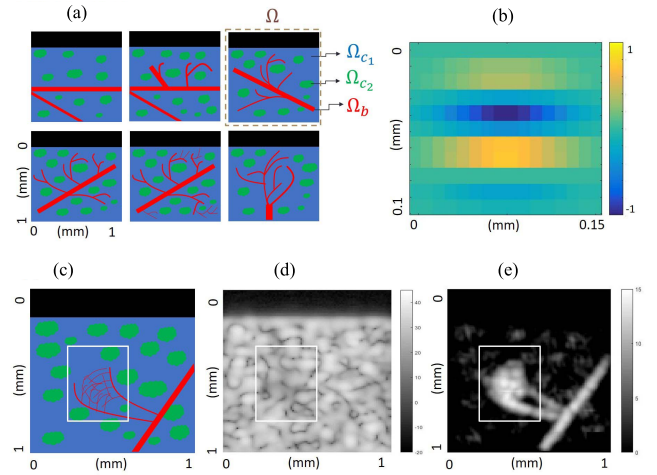


Fig. 5. Examples of training and testing fields that were used to develop a clutter filter classifier are shown with echo simulations. (a) Training fields. (b) Pulse-echo impulse response. (c) Test field. (d) Prefiltered image. (e) Postfiltered image. In (a), each of the six fields shown is composed of tissue Ω_{c_1} , Ω_{c_2} , and vascular Ω_b regions. A 15-MHz pulse-echo impulse response is illustrated in (b). For the test field in (c), the prefiltered and postfiltered PD images are shown in (d) and (e) for 15-MHz pulses. White boxes: regions containing fine vascular structures.

The j th of J data blocks is expressed as $\mathcal{X}_j \in \mathbb{C}^{\dot{N} \times \dot{M} \times \dot{L} \times \dot{K}}$, where $\dot{N} < N$, $\dot{M} < M$, $\dot{L} < L$, and $\dot{K} < K$. Each block is reshaped into $\dot{\mathcal{X}}_j \in \mathbb{C}^{\dot{N} \times \dot{S} \times \dot{K}}$, where $\dot{S} = \dot{M}\dot{L}$, and individually processed via HOSVD. The subspace selection for the j th filter is determined only by the statistical characteristics of data in that block.

III. RESULTS

A. Simulation

A primary purpose for including simulation data is to explore the clutter filter GM classifier described in Section II-E2. The classifier was trained and tested using the simulation data and then applied in the phantom and *in vivo* tumor studies shown in the following. Fig. 5(a) illustrates 6 of 12 heterogeneous regions Ω from which echo data are simulated for classifier training. The size of each field is 1 mm \times 1 mm and vessel diameters range between 10 and 100 μ m. The center frequency of pulse transmissions is either 10 or 15 MHz. Point scatterers are initially uniformly distributed in tissue regions Ω_c and vascular regions Ω_b . Tissue regions are further divided into Ω_{c_1} and Ω_{c_2} with different echogenicity. Displacements of all scatterers over time follow the tissue and blood motion functions described in Section II-C. Included in the 12 training fields, clutter-to-blood ratios were varied over the range 15 dB $< r_{CB}$ $<$ 40 dB and the blood-to-noise ratios over the range 5 dB $< r_{BN}$ $<$ 30 dB via (4). For training, 1800 data arrays were produced from the 12 regions and multiple combinations of parameters. All modeling and analysis parameters are summarized in Tables I and II.

Training and testing data are simulated using identical parameters, although the data sets are statistically independent of each other. Fig. 5(c) displays one of the testing fields. Array data are processed for HOSVD clutter filtering followed by noise filtering. Fig. 5(d) and (e) shows that vascular structures

TABLE I
ECHO DATA SIMULATION PARAMETERS

Category/Function	Parameter	Value/Range
Tissue scatterers $c_i(\cdot)$ in field Ω_{c_1}	Numbers J_{c_1}	4000
	Echo amplitude mean $\bar{\alpha}_{c_1}$	15
	Echo amplitude STD	1
Tissue scatterers $c_i(\cdot)$ in field Ω_{c_2}	Numbers J_{c_2}	1200
	Echo amplitude mean $\bar{\alpha}_{c_2}$	25
	Echo amplitude STD	1
Blood scatterers $b_i(\cdot)$ in field Ω_b	Numbers J_b	1000
	Echo amplitude mean $\bar{\alpha}_b$	1,2,3,4
	Echo amplitude STD	1
Source power ratio	Clutter-to-blood r_{CB}	15-40 dB
	Blood-to-noise r_{BN}	5-30 dB
Rigid-body motion ($\eta(t)$)	Amplitude β	0-400 μm
	Breath interval t_0	10 s
	Interval σ	0.5 s
Vibration ($\xi(t)$)	Amplitude γ	0-60 μm
	Frequency w_0	7.5 rad/s
	Direction θ	0-2 π rad
Blood flow ($\zeta(t)$)	Speed	1-3 mm/s
Pulse-echo impulse response ($h(z, y)$)	Pulse cycles	2
	Bandwidth	60 %
	F-number	1.2

TABLE II
EXPERIMENTAL PARAMETERS

Parameter	Simulation	Phantom	In-vivo Tumor
Axial samples (M)	52	100	168-272
Axial sampling rate	40.0 MHz	12.5 MHz	24.0 MHz
Axial size	1 mm	6.2 mm	5.4-8.7 mm
Slow-time samples (N)	15	17	17
Slow-time sampling rate	1.0 kHz	1.0 kHz	1.0 kHz
Frame-time samples (K)	30	30	30
Frame-time sampling rate	20 Hz	15 Hz	10-15 Hz
Scan-line numbers (L)	50	53	120-234
Scan-line density	50/mm	4/mm	16.67/mm
Lateral size	1 mm	13.2 mm	7-14 mm
Spatial samples ($S=LM$)	2.6k	5.3k	20k-64k
Sub-block size ($\tilde{N} \times \tilde{S} \times \tilde{K}$)	$17 \times 2.6k \times 30$	$17 \times 576 \times 30$	$17 \times 2.5k \times 30$
Slow-time division (J_1)	1	1	1
Spatial division (J_2)	1	15	400
Frame-time division (J_3)	1	1	1
Block numbers ($J=J_1 J_2 J_3$)	1	15	400
Classification threshold (τ)	1	1	1

are clearly visualized in the postfiltered PD map but not in the prefiltered PD map. The 50- μm vessels are not resolved at 15 MHz.

Fig. 6 provides examples from echo simulations of classification feature vector \mathbf{z} components. Fig. 6(a) shows significant overlap between the blood and clutter components, except for the largest eigenvalues where clutter dominates. Fig. 6(b) displays the first three and middle three eigen images, $\{\mathbf{S}_{i_2} | i_2 = 1, 2, 3, 21, 22, 23\}$. The first three eigen images show tissue-related speckle because their eigenvectors are mostly influenced by tissue scattering (clutter). In contrast, vessellike patterns found in the object of Fig. 5(c) appear in eigen-images 21–23, showing how those eigenvalues are dominated by vascular flow. Finally, the dip in frame-time correlation in Fig. 6(d) identifies those frames most corrupted by a rigid-body motion that simulates the effects of breathing.

1) *Errors in Blood-Signal Estimation:* Simulation enables direct error estimation as all states are known. Let fractional error be defined as $\epsilon = \|\mathbf{B} - \hat{\mathbf{B}}\|^2 / \|\mathbf{B}\|^2$ where $\|\mathbf{B}\|$ is the known blood-echo power [see (2) and (3)] and $\|\hat{\mathbf{B}}\|$ is the estimated power from (25). When the clutter and noise filters are highly effective, $\epsilon \simeq 0$. Conversely, if filters are poorly

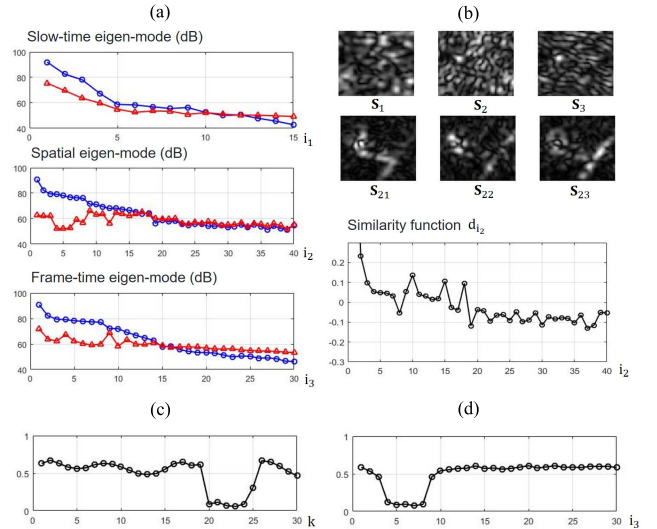


Fig. 6. Measured components of feature vector \mathbf{z} analogous to those diagramed in Fig. 4. These measurements are from echo simulations based on the test field of Fig. 5(c). (a) Contribution of the eigenvalues for clutter (\circ) and blood (Δ) signals [see (12)] is shown. Only the first 40 components of the spatial eigen mode are shown. (b) Six eigen images \mathbf{S}_1 , \mathbf{S}_2 , \mathbf{S}_3 , \mathbf{S}_{21} , \mathbf{S}_{22} , and \mathbf{S}_{23} , and the similarity measures d_{i_2} [see (13)]. (c) Mean correlation coefficients $q[k]$ between the k th frame and others [see (16)] are plotted. (d) Contribution of the i_3 th frame-time eigenvector (\mathbf{w}_{i_3}) to the rigid-motion corruption coefficient r_{i_3} [see (17)].

designed and they remove all of the blood signal, then $\epsilon \simeq 1$. Although it is possible to obtain error values greater than 1, in practice, we find $0 < \epsilon < 1$ as shown in the following.

We measure two fractional errors: ϵ_{best} computes $\hat{\mathbf{B}}$ from the training data while ϵ_{GM} computes $\hat{\mathbf{B}}$ using the testing data. Since ϵ_{best} uses exactly known training data, these errors are unavoidably generated by applying a hard threshold to data where the clutter and blood subspaces overlap. ϵ_{GM} are obtained under testing conditions and, consequently, a more practical measure of filter performance.

Fig. 7 illustrates how classification errors are influenced by clutter motion and flow speed. For the full range of conditions $\beta < 400 \mu\text{m}$, $\gamma < 60 \mu\text{m}$, and $v < 3 \text{ mm/s}$, classification errors $\epsilon_{\text{GM}} - \epsilon_{\text{best}}$ remain relatively constant between 0.1 and 0.2. However, increasing the rigid-body clutter amplitude expands the extent of the clutter subspace in the core tensor. This larger clutter eigen-bandwidth increases the overlap between the clutter and blood subspaces, thus increasing the fractional error. Alternatively, faster blood-flow speeds reduce the clutter-blood subspace overlap by shifting and expanding the blood subspace to smaller eigenvalues (larger index elements, i_3).

B. Flow Phantom

A phantom study was conducted to assess microvascular flow estimation under experimental conditions. Fig. 8 shows a dialysis cartridge containing a bundle of 0.6-mm inner diameter cellulose fibers (Spectrum Laboratories Inc., Rancho Dominguez, CA, USA). Flow in the fibers was controlled by a programmable syringe pump injecting at a constant rate either pure water for the control state or blood-mimicking (BM) fluid (CIRS, Norfolk, VA, USA) for test states. In addition,

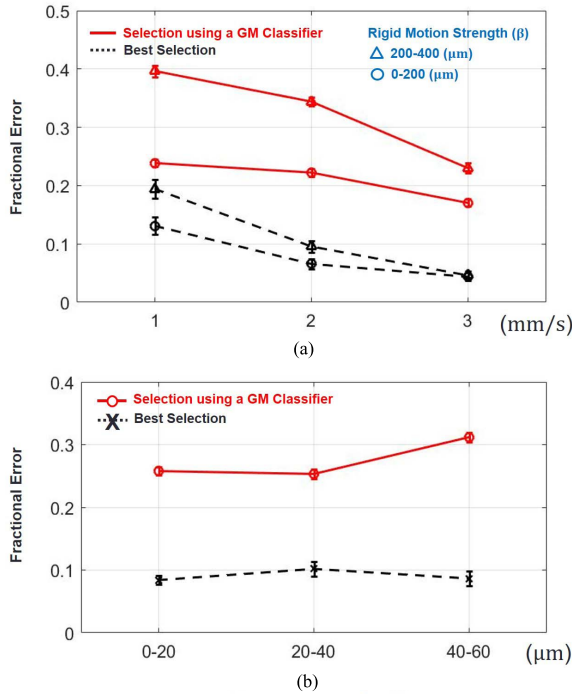


Fig. 7. Fractional errors ϵ_{GM} and ϵ_{best} as functions of (a) flow speed for clutter amplitudes β and (b) vibration strengths γ at 2-mm/s flow speed. Points and error bars denote sample means and standard deviations of the mean, respectively. Large clutter motion and slow blood speeds generate the largest classification errors because of subspace overlap.

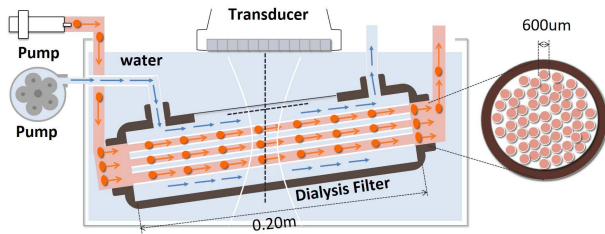


Fig. 8. Flow phantom mimicking blood circulation consists of a dialysis cartridge and two pumping systems. A syringe pump infuses either water (control state) or BM fluid (perfusion state) constantly into 0.6-mm fibers. A peristaltic pump circulates water pulses outside the fibers for clutter motion. A linear transducer scans the cartridge through an acoustic window for echo acquisition.

pulsatile water flow was generated outside the fibers using a peristaltic pump to induce sinusoidal clutter motion at frequencies between 0 and 0.5 Hz. We removed a portion of the thick plastic case protecting the cellulose fibers and wrapped that area with paraffin film (Parafilm, Bemis Company Inc., Neenah, WI, USA) to provide an acoustic window and housing structure for pulsatile clutter generation. The cartridge was immersed in degassed water for ultrasound scanning. A Vevo 2100 system with an MS200 linear array operated at 12.5 MHz (FUJIFILM VisualSonics Inc., Toronto, Ontario, Canada) was used to acquire IQ echo data in the color-flow mode for offline processing.

We compared five flow states: control state $i = 1$ has stationary water in the fibers at 0 mL/min; $i = 2$ has stationary BM fluid at 0 mL/min; $i = 3$ has BM fluid at 1 mL/min; $i = 4$ has BM fluid at 2 mL/min; and $i = 5$ has BM fluid at 3 mL/min. At each flow state, we acquired data at

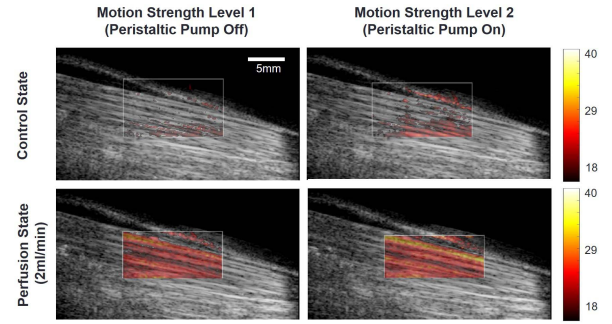


Fig. 9. PD images of 0.6-mm-diameter cellulose-fiber flow phantom at 12.5 MHz. Each is a filtered PD map superimposed on the corresponding B-mode image. Columns display two clutter levels. Rows display the control and 2-mL/min flow states. Color bar: signal power.

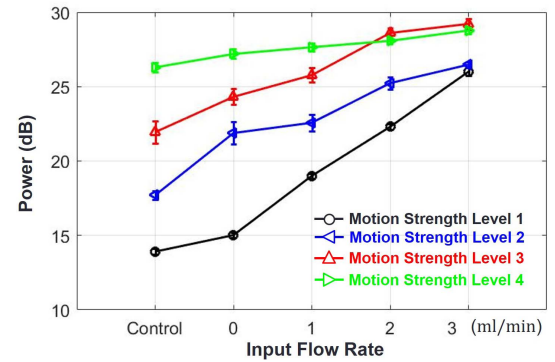


Fig. 10. Postfiltered echo power versus input flow for four clutter levels. Error bar: standard errors from averaging results of 12 acquisitions.

four clutter motion levels: $j = 1$ is no motion (peristaltic pump off), $j = 2$ is pumping with rotation frequency 0.16 Hz, $j = 3$ at 0.33 Hz, and $j = 4$ is 0.5 Hz. These values span the 12–20 breath/min range. There were 12 acquisitions recorded per state and motion level, each 2 s in duration (30 Doppler frames). PD maps \mathbf{P}_k were formed for regions 6.2 mm axially by 13.2 mm laterally (see white boxes in Fig. 9). All experimental and filter parameters are summarized in a column of Table II labeled “phantom.”

Fig. 9 displays examples of PD maps superimposed on their B-mode images for two clutter levels. Postfilter signal power was found to increase with the clutter level. The changes were quantified by computing the pixel average $s_{ijk} = (1/ML) \sum_{(m,l)} \mathbf{P}_k[m,l]$ for every PD image. Fig. 10 shows values for the 12 acquisitions, $\bar{s}_{ij} = (1/12) \sum_{k=1}^{12} s_{ijk}$, for the flow state i and the clutter motion level j . We see that the postfilter signal power (dB) increases linearly with the flow rate. Unfortunately, the rate of increase depends on the clutter motion level.

The slope change with the clutter level in Fig. 10 is consistent with our findings in the simulation results. Increasing the levels of the clutter energy for fixed flow states increases the overlap of the blood and clutter subspaces within the core tensor. The overlap is high for the slower flow velocities. Because we employ a hard threshold, the increase in postfilter signal power with the clutter level at the smallest blood speeds is expected. High-amplitude rigid-body clutter motion generates an incomplete separation of tissue and blood signals

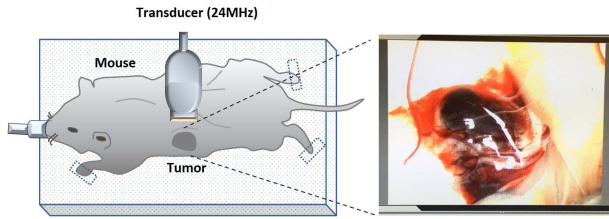


Fig. 11. Murine model of melanoma is illustrated. A mouse implanted with tumor cells is scanned in a prone position. Data are acquired at 24 MHz with the Vevo 2100 over 3 weeks.

with the effect of reducing PD image contrast as discussed in the following.

C. In Vivo Tumor Study

To further test our imaging methods, we scanned implanted mouse melanomas, *in vivo*. Tumor cells injected subcutaneously into the flank of male black C57BL/6 mice (Charles River Laboratories, Skokie, IL, USA) were investigated over time as tumors grew in size and vasculature. Fig. 11 illustrates the scan positioning. Echo data were acquired 1, 2, and 3 weeks postimplantation using the Vevo 2100 system and the MS400 transducer at 24 MHz (see Table II). Mice anesthetized with 1%–3% isoflurane is scanned to acquire 3 s of echo data (30 sequential Doppler frames at 10-Hz frame rate). The 24-MHz pulses provide high-B-mode spatial and contrast resolutions, allowing tumors to be readily located as hypoechoic regions. The clutter filter classifier that was trained using the simulation data was applied to the tumor data to identify core elements belonging to the clutter subspace. We also applied the methods of Section II-G to set velocity windows for slow flow (<4 mm/min) and fast flow (>4 mm/min) regions. The PD map was determined from the blood signal measured using (25).

Fig. 12 displays one example of low- and high-flow PD images acquired at weeks 1–3. 1 week postimplantation, the small nascent tumor appears as a hypoechoic region of the enhanced perfusion. The tumor grows rapidly after 1 week and increasing its microvascular density. This tumor has only a few larger vessels with higher velocity flows. Note that the breathing rate of the anesthetized mouse was slowed, making it easy to acquire 3 s of echo data between the breaths. In this example, the clutter was primarily from the stationary and vibrating tissues.

IV. DISCUSSION

From the simulation, phantom, and *in vivo* tumor results, we find a consistent picture regarding the performance of the clutter filter proposed for the PD imaging from a 3-D echo array. The classifier-based filter works well when the amplitude of the clutter motion is small and spatially uniform, e.g., rigid-body motion. In that case, the clutter subspace is a relatively narrowband and confined to the first few eigenstates. Consequently, the clutter and blood subspaces in \mathcal{G} are largely disjoint and, thus, the clutter subspace is readily suppressed with little effect on the blood subspace using a hard-threshold filter. In other words, the feature vector \mathbf{z} from (18) in conjunction with the classifier of (19) is able to correctly label core elements of \mathcal{G} . Our clutter filter is

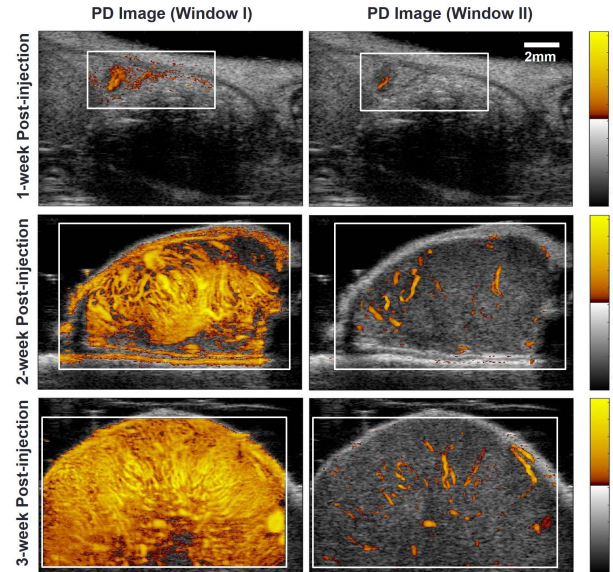


Fig. 12. PD images of a murine melanoma 1–3 weeks after implantation. Tumor size and microvasculature clearly increase with time. The left column displays PD maps of microvascular flow and perfusion for blood speeds <4 mm/min while those in the right column are flows >4 mm/min. All imaging were implemented in MATLAB 2015b on an Intel processor i5-4300U CPU, 2.50 GHz. HOSVD computation was performed using a truncation technique supported by Tensorlab toolbox [24] to minimize the running time. The time to compute all processing for one PD image (5.4 mm \times 7 mm, 1-week) is around 1 min. At 24 MHz, the blood-echo SNR is high enough to use two-cycle Doppler pulses, which enhances the spatial resolution sufficiently to see microvessels.

well designed for these tumor imaging conditions because the clutter eigen-bandwidth is narrow.

In contrast, clutter signal power in the phantom data was strongly pulsatile with a broadband clutter subspace that overlapped the TM-blood subspace. We set the filter classifier to capture all of the blood power, and as a result, the postfilter signal power contains more clutter power at slow flows than at fast flows. For this reason, the PD image contrast was reduced in Fig. 10 as more clutter power was introduced. In addition, the resistance to flow through the dialysis fibers at the lowest flow states was highly variable; we found that few fibers often carried most of the flow at higher speeds. As flow increased above 2 mL/min, flow among fibers became more uniform. In effect, the flow phantom posed more challenges to successful clutter filtering than *in vivo* tumor imaging.

To improve the clutter filtering when tissues move with high amplitude and eigen-bandwidth, we are searching for additional \mathbf{z} components that can specifically identify those physical attributes. Such features might emerge from multi-modal perfusion imaging investigations if another modality can provide appropriate independent information [14]. Alternatively, we are seeking soft-threshold decision functions that can recognize when more than one signal source is contributing to a core element. It is clear from the tumor images of Fig. 12 that peripheral microvascular imaging offers clutter conditions where our methods work very well. In these studies, the transducer was placed into a fixture so that the transducer motion relative to the tissue was only possible by breathing and not sonographer hand motions. When large rigid-body movements are present, there are preprocessing techniques

that are effective at adjusting the echo phase and amplitude to minimize the effects of large motion clutter [25].

Note that the simulation and phantom data in our report provide small-vessel flow conditions but no capillary-perfusionlike signal, the latter being characterized by the slowest and most spatially disorganized RBC movements. Both the microvascular flow and the perfusion are present in Fig. 12 as it was in a previous report involving ischemic mouse hindlimb images [15]. The perfusion is well represented in the PD spectrum that does not depend on the Doppler angle; however, unlike color-flow images, PD images offer no velocity information. We are able to obtain some speed ranging by partitioning eigenvector spectra (section II-G). We showed previously [15] that eigenvector spectral images display distinct linear patterns when RBC movement is directed, as in vessel flows, and diffuse patterns when RBC movement is disorganized, as in capillary perfusion. The 3-D eigenspace provided by HOSVD processing offers a wealth of specific information about scatterer movement that is encoded in pulse-echo signal arrays.

V. CONCLUSION

The sensitivity of PD images to tissue perfusion was increased by creating a frame-time axis in the acquired echo-data array in addition to the slow-time and spatial axes. The frame-time axis provides a high density of Doppler spectrum samples at frequencies corresponding to tissue perfusion signals. The perfusion signal was uncoupled from the tissue clutter using a 3-D SVD that generates a 3-D core tensor and three sets of eigenvectors describing the slow-time, spatial, and frame-time features of the echo signals. In this report, we describe a feature vector classifier with elements computed from the 3-D eigenspace. Three of the features report eigenvalue energy and two are similarity measures. This statistical classifier examines each core tensor element to decide if it is predominantly of clutter or nonclutter origin. Coupling the clutter filter with an acquisition noise filter and the velocity discriminator, we image the fast and slow blood-flow states *in vivo*. The blood and clutter powers are well separated for narrow eigen-bandwidth clutter signals but the overlap of these subspaces is progressively increased as the clutter eigen-bandwidth increases.

REFERENCES

- [1] J. Rubin, R. Bude, P. Carson, R. Bree, and R. Adler, "Power Doppler U.S.: A potentially useful alternative to mean frequency-based color Doppler U.S.," *Radiology*, vol. 190, no. 3, pp. 853–856, 1994.
- [2] A. C. H. Yu and L. Løvstakken, "Eigen-based clutter filter design for ultrasound color flow imaging: A review," *IEEE Trans. Ultrason., Ferroelectr., Freq. Control*, vol. 57, no. 5, pp. 1096–1111, May 2010.
- [3] S. Bjærum, H. Torp, and K. Kristoffersen, "Clutter filter design for ultrasound color flow imaging," *IEEE Trans. Ultrason., Ferroelectr., Freq. Control*, vol. 49, no. 2, pp. 204–216, Feb. 2002.
- [4] C. M. Gallippi and G. E. Trahey, "Adaptive clutter filtering via blind source separation for two-dimensional ultrasonic blood velocity measurement," *Ultrason. Imag.*, vol. 24, no. 4, pp. 193–214, Oct. 2002.
- [5] M. A. Lediju, M. J. Pihl, J. J. Dahl, and G. E. Trahey, "Quantitative assessment of the magnitude, impact and spatial extent of ultrasonic clutter," *Ultrason. Imag.*, vol. 30, no. 3, pp. 151–168, 2008.
- [6] L. Lovstakken, S. Bjærum, K. Kristoffersen, R. Haaverstad, and H. Torp, "Real-time adaptive clutter rejection filtering in color flow imaging using power method iterations," *IEEE Trans. Ultrason., Ferroelectr., Freq. Control*, vol. 53, no. 9, pp. 1597–1608, Sep. 2006.

- [7] W. C. de Albuquerque Pereira and C. D. Maciel, "Performance of ultrasound echo decomposition using singular spectrum analysis," *Ultrason. Med. Biol.*, vol. 27, no. 9, pp. 1231–1238, 2001.
- [8] F. W. Mauldin, Jr., D. Lin, and J. A. Hossack, "The singular value filter: A general filter design strategy for PCA-based signal separation in medical ultrasound imaging," *IEEE Trans. Med. Imag.*, vol. 30, no. 11, pp. 1951–1964, Nov. 2011.
- [9] C. Demeñé *et al.*, "Spatiotemporal clutter filtering of ultrafast ultrasound data highly increases Doppler and ultrasound sensitivity," *IEEE Trans. Med. Imag.*, vol. 34, no. 11, pp. 2271–2285, Nov. 2015.
- [10] J. Baranger, B. Arnal, F. Perren, O. Baud, M. Tanter, and C. Demeñé, "Adaptive spatiotemporal SVD clutter filtering for ultrafast Doppler imaging using similarity of spatial singular vectors," *IEEE Trans. Med. Imag.*, vol. 37, no. 7, pp. 1574–1586, Jul. 2018.
- [11] P. Song, A. Manduca, J. D. Trzasko, and S. Chen, "Ultrasound small vessel imaging with block-wise adaptive local clutter filtering," *IEEE Trans. Med. Imag.*, vol. 36, no. 1, pp. 251–262, Jan. 2017.
- [12] P. Song *et al.*, "Accelerated singular value-based ultrasound blood flow clutter filtering with randomized singular value decomposition and randomized spatial downsampling," *IEEE Trans. Ultrason., Ferroelectr., Freq. Control*, vol. 64, no. 4, pp. 706–716, Apr. 2017.
- [13] A. J. Y. Chee, B. Y. S. Yiu, and A. C. H. Yu, "A GPU-parallelized Eigen-based clutter filter framework for ultrasound color flow imaging," *IEEE Trans. Ultrason., Ferroelectr., Freq. Control*, vol. 64, no. 1, pp. 150–163, Jan. 2017.
- [14] J. Hedhli *et al.*, "A noninvasive lens into the functional recovery in a preclinical model of peripheral arterial disease," *Circulation*, submitted for publication.
- [15] M. Kim, C. K. Abbey, J. Hedhli, L. W. Dobrucki, and M. F. Insana, "Expanding acquisition and clutter filter dimensions for improved perfusion sensitivity," *IEEE Trans. Ultrason., Ferroelectr., Freq. Control*, vol. 64, no. 10, pp. 1429–1438, Oct. 2017.
- [16] L. De Lathauwer, B. De Moor, and J. Vandewalle, "A multilinear singular value decomposition," *SIAM J. Matrix Anal. Appl.*, vol. 21, no. 4, pp. 1253–1278, 2000.
- [17] T. G. Kolda and B. W. Bader, "Tensor decompositions and applications," *SIAM Rev.*, vol. 51, no. 3, pp. 455–500, 2009.
- [18] G. Bergqvist and E. G. Larsson, "The higher-order singular value decomposition: Theory and an application [lecture notes]," *IEEE Signal Process. Mag.*, vol. 27, no. 3, pp. 151–154, May 2010.
- [19] R. N. McDonough and A. D. Whalen, *Detection of Signals in Noise*, 2nd ed. San Diego, CA, USA: Academic, 1995.
- [20] H. L. Van Trees, *Detection, Estimation, and Modulation Theory, Part I*. New York, NY, USA: Wiley, 1968.
- [21] T. Yokota, N. Lee, and A. Cichocki, "Robust multilinear tensor rank estimation using higher order singular value decomposition and information criteria," *IEEE Trans. Signal Process.*, vol. 65, no. 5, pp. 1196–1206, Mar. 2017.
- [22] M. Wax and T. Kailath, "Detection of signals by information theoretic criteria," *IEEE Trans. Acoust., Speech, Signal Process.*, vol. 33, no. 2, pp. 387–392, Apr. 1985.
- [23] Q. Wu and D. R. Fuhrmann, "A parametric method for determining the number of signals in narrow-band direction finding," *IEEE Trans. Signal Process.*, vol. 39, no. 8, pp. 1848–1857, Aug. 1991.
- [24] N. Vervliet, O. Debals, L. Sorber, M. V. Barel, and L. D. Lathauwer. (2016). *Tensorlab 3.0*. [Online]. Available: <https://www.tensorlab.net/>
- [25] J. Tierney, C. Coolbaugh, T. Towse, and B. Byram, "Adaptive clutter demodulation for non-contrast ultrasound perfusion imaging," *IEEE Trans. Med. Imag.*, vol. 36, no. 9, pp. 1979–1991, Sep. 2017.

MinWoo Kim, photograph and biography not available at the time of publication.

Yang Zhu, photograph and biography not available at the time of publication.

Jamila Hedhli, photograph and biography not available at the time of publication.

Lawrence W. Dobrucki, photograph and biography not available at the time of publication.

Michael F. Insana, photograph and biography not available at the time of publication.